CrossMark

Hot deformation and activation energy of a CNT-reinforced aluminum matrix nanocomposite

F. Mokdad[a], D.L. Chen[a,*], Z.Y. Liu[b], D.R. Ni[b], B.L. Xiao[b], Z.Y. Ma[b,*]

[a] Department of Mechanical and Industrial Engineering, Ryerson University, 350 Victoria Street, Toronto, Ontario, M5B 2K3 Canada
[b] Shenyang National Laboratory for Materials Science, Institute of Metal Research, Chinese Academy of Sciences, 72 Wenhua Road, Shenyang 110016, China

ARTICLE INFO

ABSTRACT

Hot deformation behavior of a 2.0 wt% CNT/2024Al nanocomposite was studied via high-temperature compression over a temperature and strain rate range of 200–400 °C and 0.001–0.1 s^{-1}, respectively. Both flow stress and Zener-Hollomon parameter increased with decreasing deformation temperature and increasing strain rate. The addition of CNTs led to a significant increase of activation energy of plastic deformation, corroborating the enhanced resistance of the nanocomposite to hot deformation. This was also reflected by the increased compressive yield strength in the nanocomposite due to both Hall-Petch strengthening and effective load transfer of CNTs dispersed in the matrix with well-bonded interfaces. Detailed microstructural examinations at a high strain rate, within the upper and lower temperature limits, revealed the occurrence of second-phase particle shearing, refinement, re-precipitation, and re-orientation. The highly beneficial role of the CNT reinforcement in improving the high-temperature performance of Al alloys was discussed.

1. Introduction

Carbon nanotubes (CNTs) represent attractive reinforcements for metal matrix nanocomposites (MMNCs) due to their light weight and mechanical properties [1]. CNT reinforced aluminum matrix nanocomposites (AMNCs) have been recognized in a variety of areas such as aerospace, thermal management, and automotive sectors [2]. Several challenges still remain to overcome (e.g., low wettability, interfacial reaction, and anisotropic properties [3]). Most previous studies were performed on CNT reinforced polymer [4] or ceramic matrix nanocomposites [5,6], before interest was brought to CNT/Al nanocomposites when a few studies started to emerge about elastic-plastic responses, synthesis, and processing techniques [7,8]. 2024Al alloy has been studied by Bustamante et al. [8] when being produced by mechanical alloying and strengthened by CNT dispersion. Powder metallurgy (PM) has also been combined with friction stir processing (FSP) in [9], and well-retained layer structures of the CNTs were reported. To simulate the practical use in systems and devices, the effect of temperature on mechanical properties has been studied [10], considering some constitutive equations which relate the flow stress to strain, strain rate, and temperature [11]. Constitutive equations could be applied to predict the flow behavior of metals and alloys, while deriving the activation energy for hot deformation. For instance, Wang et al. [12] characterized the hot workability in AA7050 using activation energy and 3-D processing maps in different conditions. The compensation of strain rate during hot deformation was also taken into account in [13] when applying the constitutive model during hot deformation. The microstructural evolution and dynamic softening mechanisms of Al-Zn-Mg-Cu alloys were studied during hot compression deformation in a range of 300–450 °C and a strain rate of 0.001–0.1 s^{-1}. Flow behavior was then correlated to different microstructures and dynamic softening mechanisms [14].

Isothermal hot compression tests of as-cast and homogenized 2024Al alloys were carried out in [15] in a wide range of deformation temperatures (350–500 °C) and strain rates (0.001–10 s^{-1}), and constitutive equations were established based on the Arrhenius model. Since activation energy represents a free energy barrier for dislocations slip on slip planes and indicates the deformation resistance of materials [16,17], a deeper understanding of the relationship between activation energy and hot processing is needed. Hot workability of Al alloys using the activation energy has been previously targeted in the literature [12,18–20], as well as the true activation energy characterizing deformation mechanisms during hot working [21], however, to the authors' knowledge, the effect of CNT additions on the high-temperature performance of Al alloys is not available. No quantification on the activation energy of the nanocomposite after CNT addition has been reported. There is also no assessment on the change of second-phase particles due to CNTs. Therefore, the main objectives of this study were

to evaluate the compressive behavior at varying strain rates and temperatures, examine the microstructural features, determine the activation energy, and identify the salient strengthening mechanisms of a 2.0 wt% CNT/2024Al nanocomposite.

2. Material and experimental procedure

The 2024Al alloy powders (4.5 Cu, 1.5 Mg, 0.6 Mn in wt%, and Al (balance)) had an average diameter of ~10 μm. When fabricating the nanocomposite, these powders were mixed with 2.0 wt% CNTs of ~95–98% purity synthesized using chemical vapor deposition (CVD). CNTs were > 5 μm in length and 10–20 nm in outer diameter. The as-mixed powders of Al and CNTs were dispersed by ball milling at a rotational speed of 400 RPM with a ball powder ratio of 15:1 for 6 h. No pre-treatment was conducted on the CNTs and 2.0 wt% stearic acid was added before milling to prevent cold-working. As-milled powders were cold-compacted, degassed, and then hot-pressed at 560 °C for 1 h, and the as-pressed billets were hot extruded at 450 °C with an extrusion ratio of 25:1. The 2.0 wt% CNT/2024Al nanocomposite was finally solid solution treated at 495 °C for two hours, quenched in water at RT and then naturally aged (i.e., T4 condition). ASTM E9 standard was adopted in preparing the cylindrical specimens (Φ5 mm ×8 mm (height)), with the compression axis parallel to the extrusion direction (ED). High-temperature compression tests were performed until failure from 200 °C to 400 °C with an interval of 50 °C, at strain rates of 0.001, 0.01 and 0.1 s^{-1}, using a computerized United testing machine equipped with an environmental chamber having a temperature accuracy of ± 5 °C. After being heated up to the test temperatures, samples were held for 300 s to reach a steady deformation temperature. The strain was obtained based on crosshead displacement in the test apparatus, which included the deformation of both test sample and machine system (i.e., load train and machine frame). In evaluating the stress-strain curves, to obtain the actual deformation amount of a test sample, the deformation coming from the machine system was eliminated using a calibration curve at each temperature, which was obtained directly through the upper compression plate against the lower compression plate without any sample. Reproducibility of the results was verified by performing two tests at a given combination of strain rate and temperature. Scanning electron microscope (SEM) JSM-6380LV equipped with an Oxford energy dispersive X-ray spectroscopy (EDS) system was used to observe microstructures. EBSD analyses were carried out at a step size of 0.1 μm by means of Oxford integrated AZtecHKL advanced EBSD system with NordlysMax^2 and AZtecSynergy along with a large area analytical silicon drift detector. To characterize the initial microstructures, samples were polished via standard metallographic techniques. For the optical micrographs, microstructural features were revealed using Keller's etchant (i.e., 190 ml H$_2$O, 5 ml HNO$_3$ (65%), 3 ml HCl (32%) and 2 ml HF (40%)). No etching was done for SEM observations with the polished surfaces being examined directly. As for EBSD, sample surface was first mechanically polished, then electro-polished in an electrolyte of 10 ml nitric acid and 40 ml ethanol for about 30 s at 20 V and RT. EBSD data were analyzed by means of the AZtecHKL EBSD data acquisition software of Oxford Instruments. CNT distributions in the matrix and CNT-Al interface structures were examined using transmission electron microscopy (TEM, Tecnai G2 20) and high resolution TEM (HRTEM). The TEM samples were prepared to be parallel to the ED.

3. Results

3.1. Initial microstructure

Optical micrographs along with EBSD band contrast maps are shown in Fig. 1(a) and (b) for the 2024Al base alloy and Fig. 1(c) and (d) for the 2.0 wt% CNT/2024Al nanocomposite. Some elongated grains were visible through the micrographs parallel to the ED in both

materials. The second-phase particles were observed in both alloy and nanocomposite (Fig. 1(a) and (c)) and previously identified as Cu-containing particles (Al$_2$Cu) [22]. Based on the EBSD band contrast maps in Fig. 1(b) and (d), some elongated grains along the ED (i.e., attributed to the severe plastic deformation during extrusion) co-existed with equiaxed grains. In this context, the microstructural feature of a 0.5 wt% CNT/Al nanocomposite was observed in [23] to be highly dependent on the deformation process, and the as-sintered specimens with initial equiaxed grains were also elongated after hot extrusion. A comparison between Fig. 1(b) and (d) indicated a smaller grain size in the nanocomposite, suggesting the effective grain refinement role of CNTs. Such an effect of CNTs on the grain size was also reported in [9,24]. For instance, the grain size of a 1.0 wt% MWCNT/Ni was observed to be 47.6 μm, whereas it became only 5.3 μm for a 5.0 wt% MWCNT/Ni [24]. This was explained through the dispersion of CNTs along GBs resulting in a much finer grain size [9].

TEM examinations on the 2.0 wt% CNT/2024Al nanocomposite revealed singly dispersed CNTs in the Al matrix, as pointed by the arrows in Fig. 2(a) and (b). CNTs shorter than the received ones were observed due to the expected breakup during the fabrication of the nanocomposite, i.e., CNTs were shortened due to the shear effect during ball milling. The presence of the aluminum carbide Al$_4$C$_3$ was also detected (Fig. 2(b)), being either directly attached to CNTs or in the matrix in the vicinity of CNTs. The existence of this phase was also confirmed via XRD analysis in our earlier study [22]. This suggests the occurrence of reaction between Al and CNTs to some extent in the fabrication process, where carbon atoms would react with Al at high temperatures at some defect locations [9]. The formation of Al$_4$C$_3$ could also be related to the shortening of CNTs which could eventually lead to an increasing number of carbon atoms at the CNT tips and thus increase the probability of CNT-Al reactions during severe plastic deformation at high temperatures. HRTEM images showed the interface features between CNTs and Al matrix (Fig. 2(c)), where it can be seen that the CNT-Al interface was densely bonded and no voids or defects were detected. Also, the layered multi-walled CNT structure and the inter-layer distance between CNT walls were visible in Fig. 2(c). The HRTEM image displayed in Fig. 2(d) confirmed the presence of the plate-like Al$_4$C$_3$ along the (003) plane. The coherent interface in the direct bond between the matrix and the reinforcement would increase the effectiveness of load transfer and the resulting strength of the nanocomposite. In fact, at the atomic level a strong cohesion between the matrix and nano-sized CNTs can be attained, and depending on the volume fraction, CNTs would carry a certain portion of the load between matrix and reinforcement.

3.2. Compressive behavior

Fig. 3 shows the true stress-true strain compression curves of the base alloy and nanocomposite obtained at different temperatures and strain rates. In Fig. 3(a) deformation temperatures were varied (i.e., 200, 250, 300, 350 and 400 °C) at a fixed strain rate of 0.001 s^{-1}, whereas in Fig. 3(b) tests were conducted at 300 °C while varying the strain rates (i.e., 0.1, 0.01, and 0.001 s^{-1}). It is seen that the flow stress increased considerably with decreasing temperature and increasing strain rate. A comparison between both plots affirms that the deformation temperature had a stronger effect on the flow stress of both materials than the strain rate. Also, a saturation level was attained in most cases. When comparing the behavior of both materials at a given strain rate and temperature (Fig. 3(a) and (b)), the strengthening behavior brought by the addition of CNTs was clearly demonstrated due to the effective load transfer (or load-carrying capacity) of CNTs dispersed in the matrix stemming from their well-bonded interfaces. This was also attributed to the Hall-Petch strengthening, also known as the GB strengthening where the material is strengthened by refining its average grain size due to the interaction between dislocations and GBs [25]. Hall-Petch strengthening is partially related to the CYS augmenta-
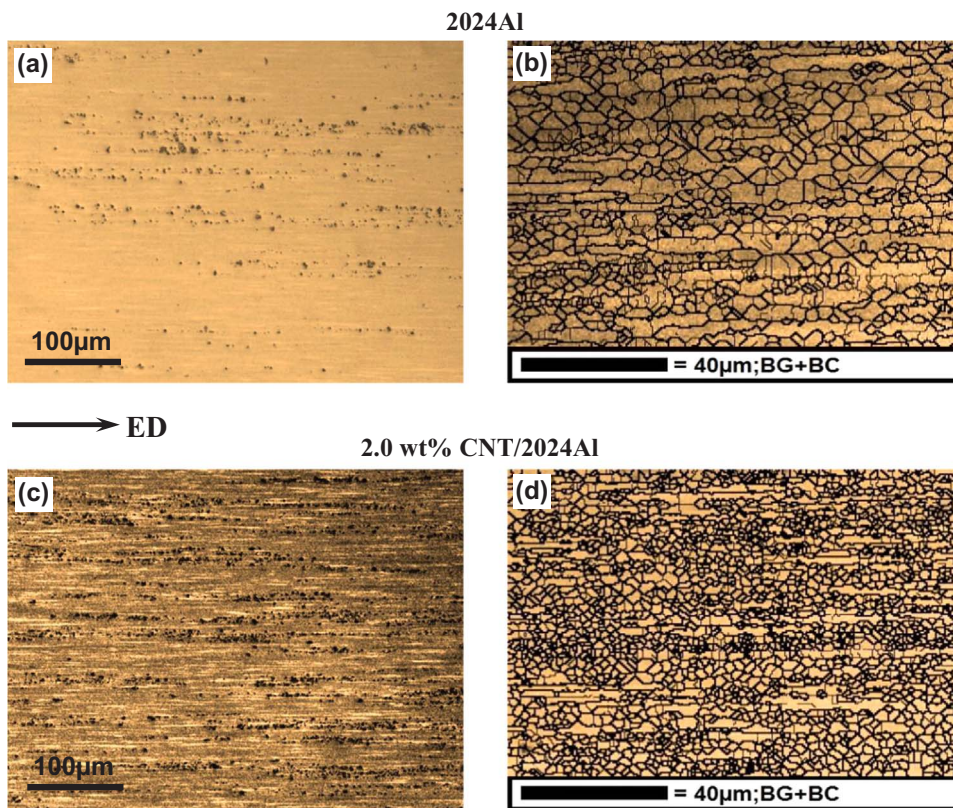
2024Al

Fig. 1. Optical micrographs and EBSD band contrast maps of (a, b) the 2024Al alloy, and (c, d) the 2.0 wt% CNT/2024Al nanocomposite, respectively.
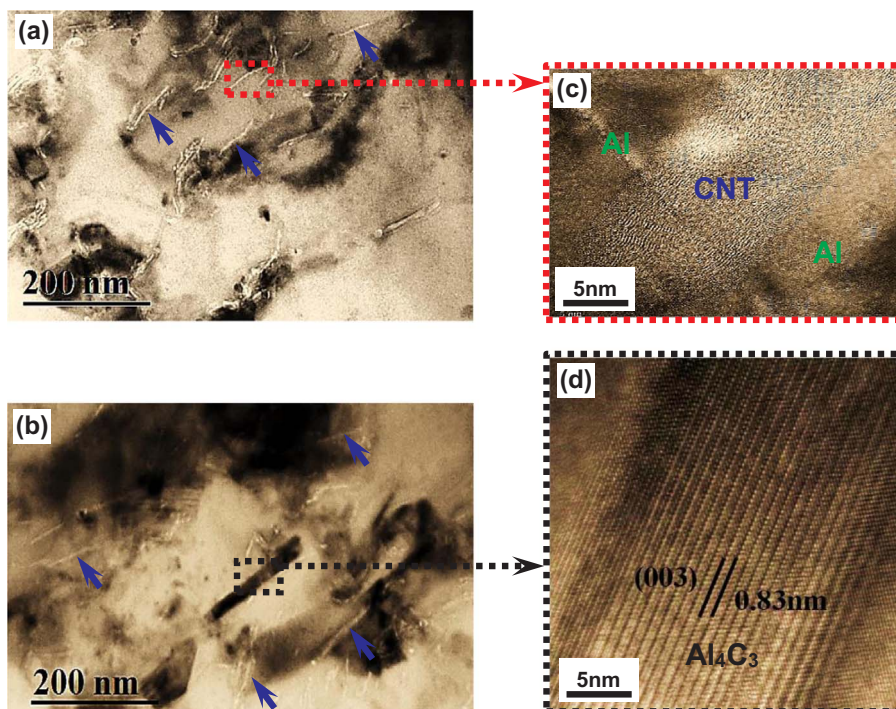

Fig. 2. Typical TEM images of the 2.0 wt% CNT/2024Al nanocomposite, indicating (a) singly dispersed CNTs, and (b) the formation of Al_4C_3 phase; HRTEM images displaying (c) a magnified singly dispersed CNT in the box shown in (a), and (d) an Al_4C_3 compound in the box shown in (b).

tion observed especially at lower temperatures, where the nanocomposite is strengthened more by grain refinement [26] compared to the base alloy as observed in the EBSD band contrast maps of Fig. 1(b) and (d). In fact, the motion of dislocations during deformation is impeded by GBs, which act as pinning sites, barring the dislocation movement and multiplication, and causing pile-ups of dislocation clusters [27].

The smaller the grain size is, the more GBs are present, thus leading to a more difficult dislocation movement and a higher flow stress for the nanocomposite.

The enhancement in the flow resistance by the addition of CNTs was observed in [28] while studying nanocomposites with different volume fractions of MWCNTs (e.g., 1.5, 3, 4.5 and 6 vol%) at different
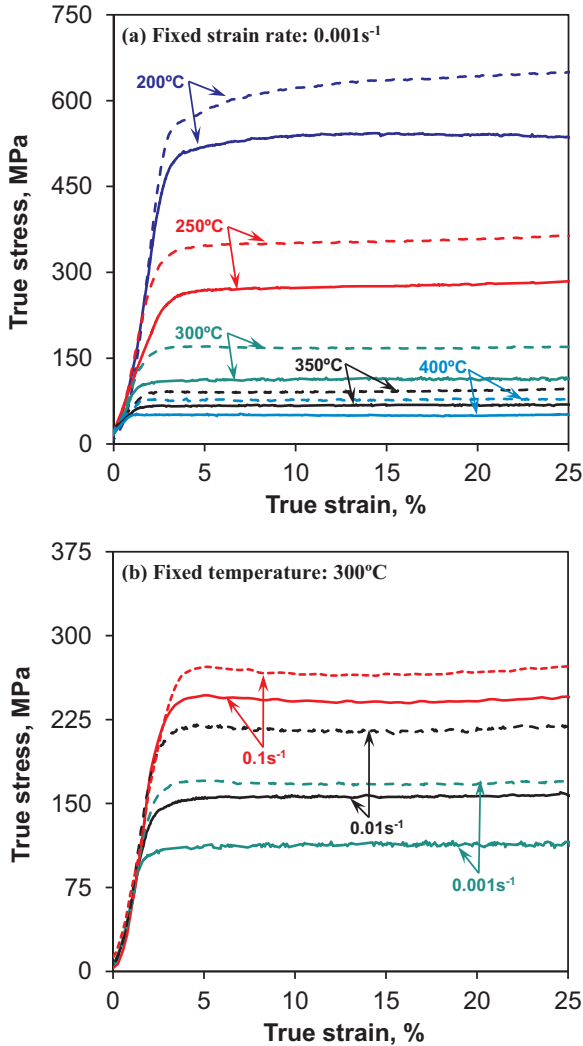
Fig. 3. Compressive true stress-true strain curves of the 2024Al alloy (continuous lines) and the 2.0 wt% CNT/2024Al nanocomposite (dashed lines), (a) at a strain rate of 0.001 s^{-1} and varying temperatures, and (b) at 300 °C and varying strain rates.

temperatures. It was observed that the higher the vol% of the CNTs was, the higher the flow resistance was at elevated temperatures. The evaluated CYS in Fig. 3 decreased with increasing temperature at all strain rates, which was attributed to the augmented thermal activation of the nanocomposite and the kinetic energy of the metal matrix which boosted the dislocation movements at higher temperatures [29]. Some factors related to the fabrication process could also have contributed to the enhancement of the flow behavior of the alloy and nanocomposite, mainly ball milling, which resulted in a more refined microstructure along with a uniform distribution of CNTs. In addition, the spontaneous reaction between Al and O_2 when exposed to air during milling of the 2024Al powders, could lead to the formation of Al_2O_3 oxides. These particles were then dispersed in the 2024Al matrix after extrusion, inducing a further increase in strength according to the Orowan strengthening mechanism [30,31].

3.3. Constitutive modeling

The relationship between strain rate, deformation temperature, and flow stress was extensively used by means of Arrhenius equation, which could be expressed as [32]:

$$\dot{\varepsilon} = A\left[\sinh(\alpha\sigma)\right]^n \exp\left(-\frac{Q}{RT}\right), \tag{1}$$

where n and A are material constants, α is a stress multiplier, σ is the flow stress (MPa), Q is the activation energy for hot deformation (kJ/mol), R is the universal gas constant (8.314 J/mol-K), and T is the deformation temperature (K). At high and low stress levels, the relationship between the flow stress and strain rate could be described by [33]:

$$\dot{\varepsilon} = A_1 \sigma^{n_1} \exp\left(-\frac{Q}{RT}\right), \tag{2}$$

$$\dot{\varepsilon} = A_2 \exp(\beta\sigma)\exp\left(-\frac{Q}{RT}\right), \tag{3}$$

where A_1 and A_2 are the material constants. By taking the natural logarithm on both sides of Eqs.(2) and (3), we have,

$$\ln\dot{\varepsilon} = \ln A_1 + n_1 \ln\sigma - \frac{Q}{RT}, \tag{4}$$

$$\ln\dot{\varepsilon} = \ln A_2 + \beta\sigma - \frac{Q}{RT}. \tag{5}$$

The term σ is substituted in the current study by the CYS values. Data obtained at different deformation temperatures (i.e., 200, 250, 300, 350, and 400 °C) were used to calculate the activation energy for the alloy and nanocomposite. Fig. 4(a) shows the plot of $\ln\dot{\varepsilon}$ vs. $\ln\sigma$ for both alloy and nanocomposite. A linear relationship was noted in both cases having the slope n_1 in Equ.(4). Fig. 4(b) displays the relation between $\ln\dot{\varepsilon}$ and σ for both materials. A linear trend also appeared, which was characterized by the slope β in Equ.(5). Average slope values over the range of deformation temperatures were used to calculate n_1 and β. The stress multiplier α could be estimated as $\alpha=\beta/n_1$. The obtained values of n_1, β, and α for the alloy and nanocomposite were summarized in Table 1. Being back to Equ.(1), and taking the natural logarithm on both sides, one can obtain,

$$\ln\dot{\varepsilon} = \ln A + n \ln\left[\sinh(\alpha\sigma)\right] - \frac{Q}{RT}. \tag{6}$$

Fig. 4(c) shows the plot of $\ln\dot{\varepsilon}$ vs. $\ln(\sinh(\alpha\sigma))$ where a linear trend was also exhibited for both materials, which was represented by an average slope n. The obtained values of n for both alloy and nanocomposite were also included in Table 1.

3.4. Activation energy of hot deformation

The activation energy, Q, is generally related to the thermodynamic mechanism of dislocation movement and can reveal the workability of materials [18]. It is in fact a measure of the minimum energy required to initiate dislocation movement by diffusion, and is considered to be an important physical parameter indicating the degree of difficulty to deform a material under specific deformation conditions [34]. Activation energy could be determined after taking partial differential of Eq. (6), then the following could be obtained,

$$Q = R\left[\frac{\partial \ln\dot{\varepsilon}}{\partial \ln\left[\sinh(\alpha\sigma)\right]}\right]_T \cdot \left[\frac{\partial \ln\left[\sinh(\alpha\sigma)\right]}{\partial(1/T)}\right]_{\dot{\varepsilon}} = RnS, \tag{7}$$

The newly introduced parameter S in Equ.(7) is the average slope of the $\ln\left[\sinh(\alpha\sigma)\right] - 1/T$ plot at various strain rates (Fig. 5(a) and (b) for the alloy and nanocomposite, respectively). The obtained values of S for the 2024Al and 2.0 wt% CNT 2024Al nanocomposite are also listed in Table 1. Activation energy Q could thus be calculated based on Equ.(7) and was obtained to be 274.5 kJ/mol for the base alloy and 322.3 kJ/mol for the nanocomposite. As expected, both values were higher than that for self-diffusion of pure aluminum [35] due to the influence of alloying elements and the CNT addition on the thermos-mechanical properties of alloy and nanocomposite. Different values have been reported in the literature for the activation energy of Al alloys, for instance, Wang et al. [12] reported that for the AA7050 alloy it could go as high as 470.2 kJ/mol at 330 °C and a strain rate of 0.001 s^{-1}, and as
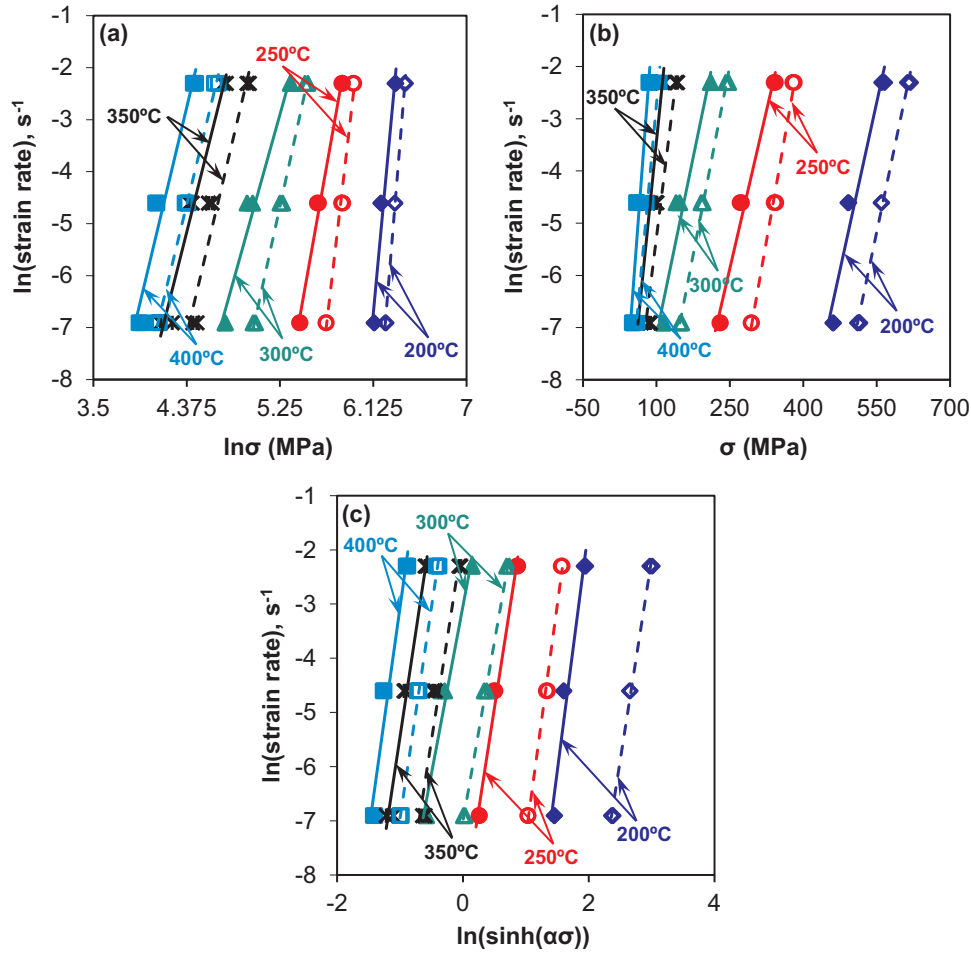
Fig. 4. The relationship of CYS, strain rate and temperature of the base 2024Al alloy (continuous lines) and the 2.0 wt% CNT/2024Al (dashed lines): (a) ln ($\dot{\varepsilon}$) versus *ln (σ)*, (b) ln ($\dot{\varepsilon}$) versus *σ*, and (c) *ln($\dot{\varepsilon}$)* versus *ln[sinh(ασ)]*.

Table 1
Main parameters of the hot deformed 2024Al alloy and 2.0 wt% CNT/2024Al nanocomposite evaluated from the constitutive equations.

	n_1	β	α	n	S	Q, kJ/mol
2024Al	13.84	64.88×10^{-3}	4.68×10^{-3}	7.15	4.61	**274.5**
2.0 wt% CNT/ 2024Al	11.53	69.04×10^{-3}	5.98×10^{-3}	7.09	5.46	**322.3**

low as 82.8 kJ/mol at 420 °C and 10 s^{-1}. A similar temperature range to the current study (200–400 °C) was considered in [36] and an activation energy of 282.6 kJ/mol was reported for an Al-Si alloy, which is comparable to the obtained value for the 2024Al alloy (274.5 kJ/mol). The alloy studied in [36] was then modified by adding transition alloying elements V and Zr, leading to a higher activation energy of 315.2 kJ/mol. Likewise, the addition of CNTs in the 2024Al alloy enhanced the activation energy to 322.3 kJ/mol. Compared to the base alloy, due to the presence of CNTs, dislocations were pinned by the nanoparticles and encountered friction drags. Both thermal energy and external stresses required for dislocation motion increased [20]. The presence of finer particles is therefore effective for the increase of activation energy. In this context, Ko and Yoo [19] studied the activation energy of a SiC$_p$ reinforced 2024Al while varying the size of the reinforcement (1 and 8 μm in diameter), and reported that coarser SiC$_p$ particles of 8 μm led to Q = 290.3 kJ/mol (in the 470–500 °C range), while finer particles of 1 μm helped achieve Q

= 395.3 kJ/mol, suggesting the complexity of dislocation interactions caused by the rigid SiC$_p$ reinforcement of smaller diameters during hot deformation. This observation corroborated the increase in Q due to CNT addition in the present study. Malas *et al.* [35] compared the activation energy of (1) wrought 2024Al, (2) powder metallurgy 2024Al, and (3) PM 2024Al with SiC whiskers (SiC$_w$). The following value ranges for Q were reported for the enumerated materials: (1) [90–200] kJ/mol, (2) [167–418] kJ/mol, and (3) [377–1047] kJ/mol. First, it is clear that the obtained value for the 2024Al (Q=274.5 kJ/mol) falls within the PM 2024Al value range (i.e., ball milling in the current study). The second observation is about the significant increase in the values of Q due to SiC$_w$ reinforcement, although greater values were observed compared with the current 2.0 wt% CNT/2024Al nanocomposite (Q=322.3 kJ/mol). The higher values obtained for the SiC$_w$ could be expected since it involves rigid ceramic particles in a plastically deformed 2024Al matrix [35].

3.5. Zener-Hollomon parameter

The effects of strain rate and deformation temperature could be represented by a single parameter as a function of flow stress, namely the Zener-Hollomon parameter (Z), defined as [34,36,37],

$$Z = \dot{\varepsilon} \exp\left(\frac{Q}{RT}\right). \tag{8}$$

The obtained values of the Z parameter for various deformation temperatures and strain rates were summarized in Table 2 for the 2024Al alloy and in Table 3 for the 2.0 wt% CNT/2024Al nanocompo-
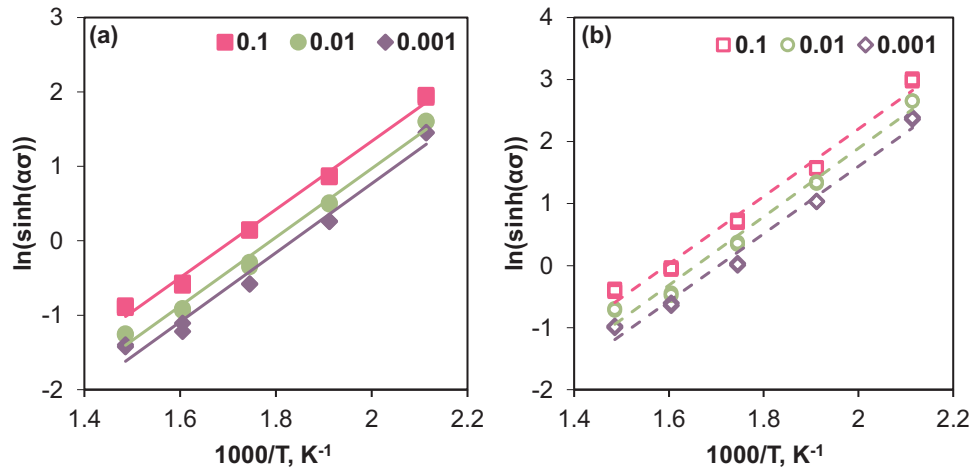
Fig. 5. Relationship between CYS, strain rate and temperature in terms of $ln[sinh(\alpha\sigma)]$ versus $1000/T$ for (a) 2024Al alloy and (b) 2.0 wt% CNT/2024Al nanocomposite, where the train rates are expressed in s^{-1}.

Table 2
The calculated Zener-Hollomon parameter of the 2024Al alloy at different strain rates and temperatures.

Strain rate, s^{-1}	Zener-Hollomon parameter (Z)				
	Temperature, ˚C				
	200	250	300	350	400
0.001	2.1×10^{27}	2.6×10^{24}	1.1×10^{22}	1.04×10^{20}	2.02×10^{18}
0.01	2.1×10^{28}	2.6×10^{25}	1.1×10^{23}	1.04×10^{21}	2.02×10^{19}
0.1	2.1×10^{29}	2.6×10^{26}	1.1×10^{24}	1.04×10^{22}	2.02×10^{20}

Table 3
The calculated Zener-Hollomon parameter of the 2.0 wt% CNT/2024Al nanocomposite at different strain rates and temperatures.

Strain rate, s^{-1}	Zener-Hollomon parameter (Z)				
	Temperature, ˚C				
	200	250	300	350	400
0.001	3.9×10^{32}	1.5×10^{29}	2.4×10^{26}	1.1×10^{24}	1.04×10^{22}
0.01	3.9×10^{33}	1.5×10^{30}	2.4×10^{27}	1.1×10^{25}	1.04×10^{23}
0.1	3.9×10^{34}	1.5×10^{31}	2.4×10^{28}	1.1×10^{26}	1.04×10^{24}

site. As shown in Fig. 6(a), the Z values increased with increasing strain rate and decreasing temperature for the base alloy. Although the nanocomposite showed a similar trend of changes (Fig. 6(b)), the Z values were higher than that for the base alloy in all test conditions. A linear relationship between ln$Z$ and ln [$sinh(\alpha\sigma)$] could be plotted for the alloy and nanocomposite, as shown in Fig. 7, and it confirmed that at lower temperatures and higher strain rates the higher Z values corresponded to higher strengths. However, at higher temperatures and lower strain rates Z exhibited lower values, which reflected the occurrence of dynamic recrystallization, giving rise to a decrease in the strength of the alloy [34]. A similar trend was reported by Jin *et al.* [20] during hot compression of the AA7150 wrought alloy tested at different strain rates and temperatures.

4. Discussion

4.1. 2024Al deformed at 200 ˚C and 0.1 s^{-1}

Fig. 8(a) presents a typical SEM micrograph showing the overall microstructural features of the 2024Al alloy deformed at a strain rate of 0.1 s^{-1} and 200 ˚C. A major crack was observed in the micrograph. Micro-cracks were observed to propagate in the magnified region displayed in Fig. 8(b) and to interact with second-phase particles, where the crack nucleated and propagated due to the presence of stress concentration caused by nonhomogeneous deformation at higher strain rates (0.1 s^{-1}). As for Fig. 8(c), the presence of voids (i.e., pointed by
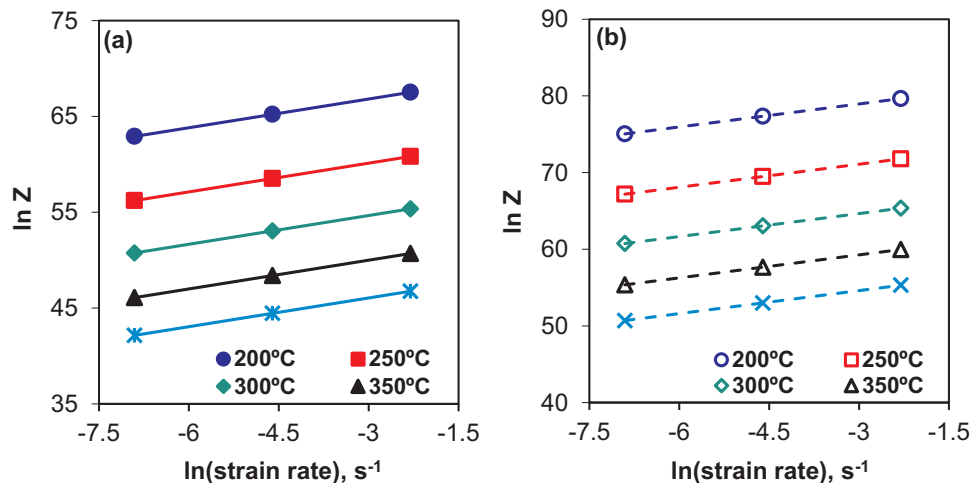

Fig. 6. Relationship between lnZ and ln ($\dot\varepsilon$) at different temperatures for (a) the 2024Al alloy and (b) the 2.0 wt% CNT/2024Al nanocomposite.
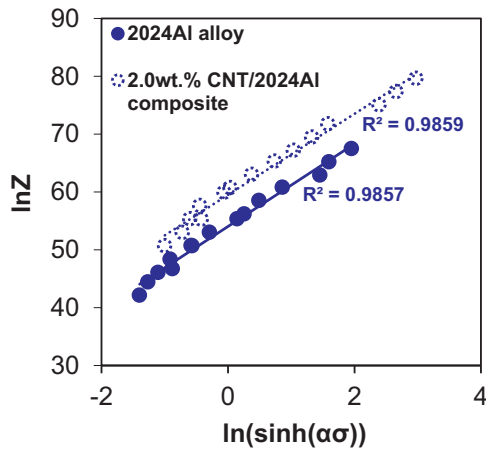
Fig. 7. Relationship between ln$Z$ and ln[$sinh(\alpha\sigma)$] for the 2024Al alloy and 2.0 wt% CNT/2024Al nanocomposite.

arrows) was detected. These voids were generated between the "soft" matrix and the "hard" particles, initiating macroscopic cracks from the surface to the interior linking to the voids. Cracking was also attributed to considerable stress concentration, caused by the sliding of neighboring grains under shear stress, where some micro-cracks occurred near the specimen surface and continued to propagate by coalescence.

4.2. Particle cracking for the 2024Al

Fig. 9(a) presents a magnified view of the second-phase particle in Zone 1 of Fig. 8. As previously found [22], coarser particles observed in the 2024Al were identified as Al$_2$Cu. Several cracks were observed to occur in Fig. 9(a) and tended to be parallel to the macroscopic compression axis (along ED), indicating that fracture was caused by local shear stresses. As schematized in Fig. 9(b), major and minor cracks could be distinguished. The major cracks led to the lateral shift of the upper portion of the particle (part 1 in Fig. 9(b)) parallel to the

compression axis (CD). This could be attributed to the shear via the motion of multiple dislocations along primary slip planes [38]. When increasing larger compressive stresses are applied, parts 1 and 2 in Fig. 9(b) are expected to fully detach giving the illusion of the formation of two finer particles. This assumption will be further elaborated in the coming section. Minor cracks illustrated in Fig. 9(b) (part 2) could be attributed to the accumulated shear stresses near the particle in the same manner.

4.3. Al$_2$Cu particles in 2024Al deformed at 400 °C and 0.1 s^{-1}

Fig. 10(a) presents the SEM micrograph of the undeformed 2024Al, and Fig. 10(b) shows the deformed microstructure for the sample compressed at 400 °C and 0.1 s^{-1}. Morphological changes of the second-phase particles occurred in terms of size and dispersion in the Al matrix since particles at 400 °C were "softer" and easier to be cut through by dislocations than those at 200 °C (Fig. 9). Hence the shearing of the Al$_2$Cu particles, by pairs of dislocations moving on the primary slip planes was faster. During continued high-temperature compression at 400 °C, the size of the particles would be expected to reduce considerably since they presented very little or no resistance to the movement of dislocations [38]. It was also reported in [39] that during hot deformation moving dislocations were repeatedly locked and unlocked by the dynamic precipitates leading to continuous shear. Such shearing has indeed been seen to start even at 200 °C (Fig. 9), where local shear stresses led to the parting of the particles. It is expected that the extent of shearing of softer particles during hot deformation at higher temperatures (400 °C) would be much higher, leading to a uniform distribution of fine particles (Fig. 10(b)).

Based on the Al-Cu binary phase diagram, if an alloy with the composition of Al-4.5 wt%Cu is heated to the temperature of ~548 °C, all copper would be dissolved in the solid solution as an FCC phase. The solid solution would then become supersaturated with Cu at lower temperatures and the driving force for precipitation would lead to the formation of Al$_2$Cu phase [40]. It was also reported in [41] that when Al-Cu alloys are exposed to high temperatures (i.e., corresponding to
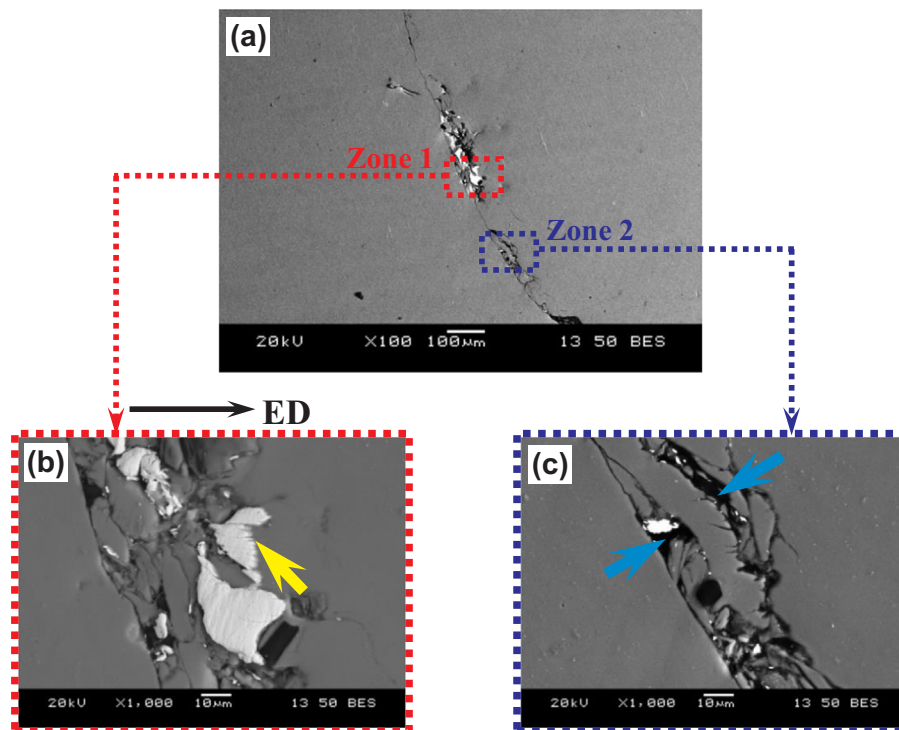

Fig. 8. Typical SEM micrograph showing (a) the overall microstructural features of the 2024Al alloy deformed at a strain rate of 0.1 s^{-1} and 200 °C, along with magnified micrographs of (b) zone 1 and (c) zone 2.
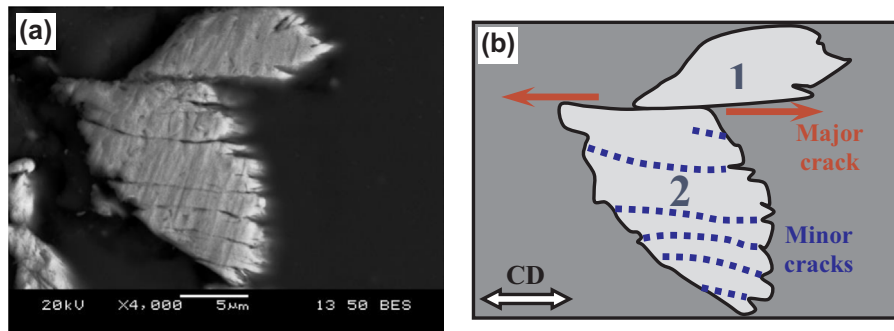
Fig. 9. s-phase particle shearing in the 2024Al base alloy compressed at 0.1 s^{-1} and 200 ℃: (a) SEM micrograph, and (b) schematic representation.
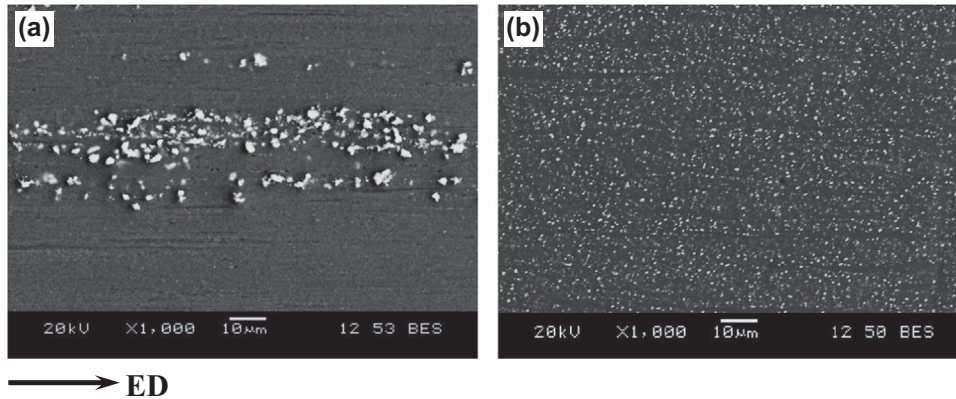

Fig. 10. Comparison between the SEM micrographs of the 2024Al alloy (a) in the undeformed state, and (b) after compression at 0.1 s^{-1} and 400 ℃.

the maximum safe limits relative to the lowest melting point for each specific composition), soluble phases formed during solidification could be re-dissolved in the matrix. Depending on the alloy composition, the complete dissolution of the intermetallics formed between alloying elements may not be possible [41]. Based on this, another explanation for the formation of microstructures in Fig. 10(b) would be: The Al$_2$Cu second-phase particles might have partially dissolved in the Al matrix at 400 ℃; then about 2 wt% Cu (based on the Al-Cu binary phase diagram at 400 ℃) would "re-precipitate" into the Al matrix to form fine Al$_2$Cu particles. Once samples got back to RT, further re-precipitates of smaller sizes would be uniformly distributed, such as the case of Fig. 10(b). Differential scanning calorimetry (DSC) was run in [41] for Al-Si-Mg-Cu alloys, the first major endothermic peak was observed at 510 ℃ and was related to the dissolution of the Al$_2$Cu phase during solution treatment. However, solution treatment remains a static transformation and particles would behave differently during dynamic deformation at high temperatures, due to their continuous moving and

mixing. This led to the consideration of partial dissolution and re-precipitation for the samples deformed at 400 ℃, which would result in the formation of fine, uniformly distributed spherical θ-phase particles.

4.4. 2.0 wt% CNT/2024Al deformed at 200 ℃ and 0.1 s^{-1}

Fig. 11(a) presents the SEM micrograph of the 2.0 wt% CNT/2024Al nanocomposite deformed at a strain rate of 0.1 s^{-1} and 200 ℃. In addition to crack propagation through the observed surface, void formation in the nanocomposite was noted, as pointed by the arrows in Fig. 11(a). This was expected to cause the reduction of workability of the nanocomposite due to cavity formation, eventually contributing to ductile fracture [39]. From the magnified view of Fig. 11(b), two types of cracking were observed: Minor cracks propagating along the ED (i.e., compression direction) and were indicated by the thin red arrows in Fig. 11(b), and major cracks having an orientation at ~45° to the ED, pointed by the thick green arrows in Fig. 11(b). The nature of these
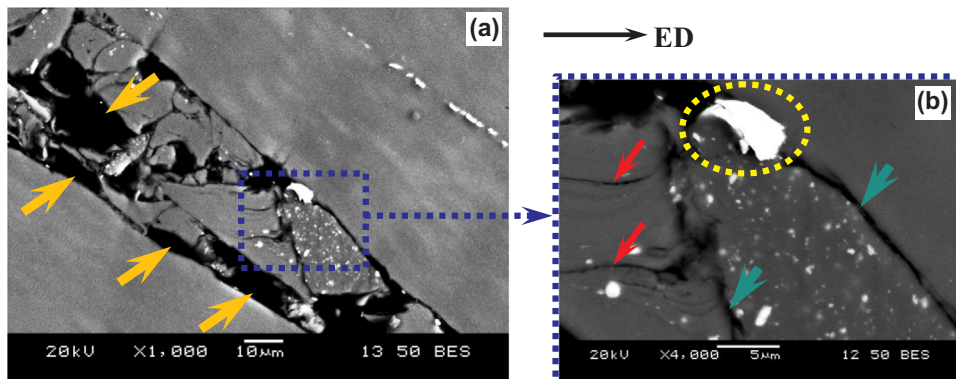

Fig. 11. Typical SEM micrograph showing (a) microstructural features of the 2.0 wt% CNT/2024Al nanocomposite deformed at a strain rate of 0.1 s^{-1} and 200 ℃, along with a magnified view in (b).

cracks could be linked to the difference of loading along the ED, caused by the significant difference in the elastic moduli between the matrix and CNTs. This would induce stress concentrations and inhomogeneous flow of the 2024Al matrix, thus leading to the deep major cracks inclined at ~45° to the applied stress direction, and the minor shear cracks parallel to the ED. The deformation stress generated near the SiC$_P$-matrix interface was also studied in [42] for the 20 vol% SiC$_P$/2024Al nanocomposite. It was concluded that if deformation stress generated near the matrix/reinforcement interface does not have enough time to be accommodated and exceeds the strength of the interface, cavities would occur, grow, coalesce, and cause damage. Another observation could be made where the second-phase particle, shown by dashed oval in Fig. 11(b), displayed enhanced strength and resistance when compared to the particle previously studied in Fig. 9. This was assumed based on the structure of the particle which did not allow the propagation of as many cracks as in Fig. 9(i.e., only one crack could be identified in the particle in Fig. 11(b)). A similar observation was also reported in [36] where precipitates of the reinforced Al-Si alloy were observed to be stronger than those in the base alloy and less frequent cracking was observed, leading to a substantially lower fraction of cracked particles in the reinforced alloy, similar to the present case of the 2.0 wt% CNT/2024Al.

4.5. Precipitate rotation in the 2.0 wt% CNT/2024Al

Fig. 12(a) presents the SEM micrograph of the 2.0 wt% CNT/2024Al sample compressed at 400 °C and 0.1 s^{-1}. A clear rotation of second-phase particles was noted with respect to the compression direction (or ED shown in Fig. 12). As schematized in Fig. 12(b), an angle θ could be defined between the loading direction and the particle alignment direction to indicate the material flow during hot deformation. A rotation of the Si particles was also observed for the Al-6-65Si-0.44Mg reinforced with B$_4$C particles, where the particle alignment after compression reflected the material flow [43]. The orientation distribution of the eutectic Si particles after compression at a strain rate of 1 s^{-1} and 400 °C was also provided in [36] where the fraction of precipitates and precipitate orientation based on the angle formed with the loading direction were quantified. Re-orientation of the particles with increasing deformation temperature was accompanied by eventual void nucleation, growth and coalescence, which was similar to the presence of some voids seen in Fig. 12(a) and further magnified in Fig. 12(c).

5. Conclusions

TEM examinations revealed singly dispersed CNTs in the matrix and well-bonded interfaces between the matrix and CNTs, although the shortening of CNTs was observed to occur due to ball milling.

1) Flow stress of both alloy and nanocomposite increased with decreasing deformation temperature and increasing strain rate, which corresponded well to the change of Zener-Hollomon parameter.
2) The high-temperature deformation resistance represented by the compressive yield strength (CYS) of the nanocomposite was effectively enhanced owing to the addition of CNTs.
3) The presence of CNTs in the nanocomposite increased the activation energy of plastic deformation from 274.5 kJ/mol to 322.3 kJ/mol, suggesting the highly beneficial role of the reinforcement in improving the high-temperature performance.
4) Second-phase Al$_2$Cu particles exhibited characteristic behavior depending on deformation temperatures and strain rates. Extensive shearing by the motion of dislocations was observed, leading to shear cracking or total particle partitioning, thus refining the particles especially at higher temperatures. Partial dissolution and re-precipitation occurred at higher temperatures, and second-phase particles were observed to be aligned along the material flow direction during hot deformation in the nanocomposite.
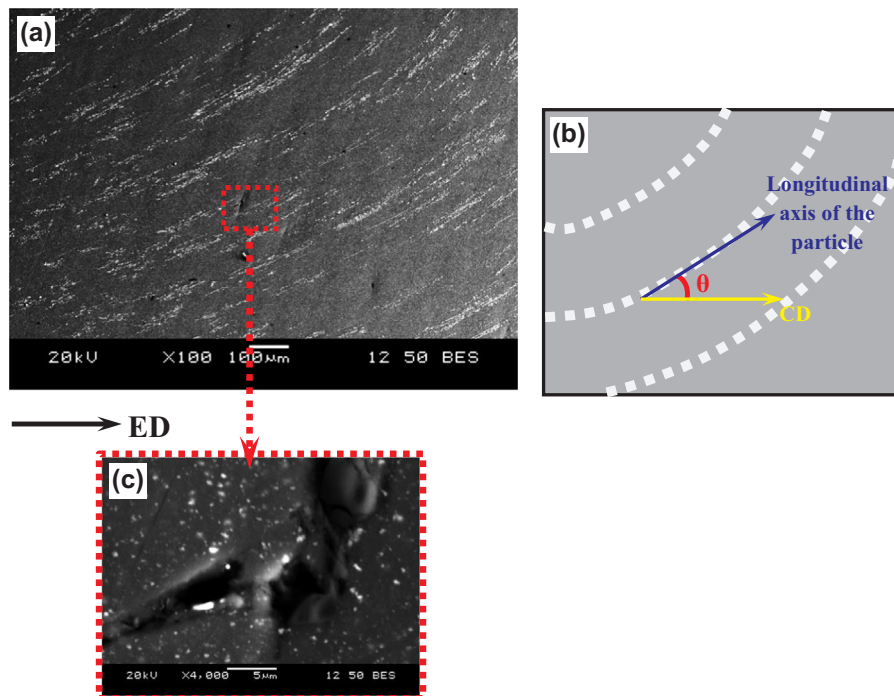
Fig. 12. Typical SEM micrograph showing (a) second-phase particle rotation of the 2.0 wt% CNT/2024Al nanocomposite deformed at a strain rate of 0.1 s^{-1} and 400 °C, (b) schematic representation, and (c) a magnified view of a zone boxed in (a).

References

[1] N. Behabtu, C.C. Young, D.E. Tsentalovich, O. Kleinerman, X. Wang, W. Anson, et al., Strong, light, multifunctional fibers of carbon nanotubes with ultrahigh conductivity, Science 339 (2013) 182–186.

[2] M.M. Shulaker, G. Hills, N. Patil, H. Wei, H.Y. Chen, H.S.P. Wong, S. Mitra, Carbon nanotube computer, Nature 501 (2013) 526–530.

[3] Y. Huang, Q. Ouyang, D. Zhang, J. Zhu, R. Li, H. Yu, Microstructures and tensile properties of ultrafine-grained Ni–(1–3.5) wt% SiCNP composites prepared by a powder metallurgy route, Acta Metall. Sin. 27 (2014) 775–786.

[4] L. Feng, K.Z. Li, Z.S. Si, Q. Song, H.J. Li, J.H. Lu, et al., Compressive and interlaminar shear properties of carbon/carbon composite laminates reinforced with carbon nanotube-grafted carbon fibers produced by injection chemical vapor deposition, Mater. Sci. Eng. A 626 (2015) 449–457.

[5] L. Longbiao, Damage evolution of cross-ply ceramic-matrix composites under stress-rupture and cyclic loading at elevated temperatures in oxidizing atmosphere, Mater. Sci. Eng. A 688 (2017) 315–321.

[6] Z. Sun, H. Shao, X. Niu, Y. Song, Failure simulation of unidirectional fiber-reinforced ceramic matrix composites based on evolving compliant interfacial debonding model, Mater. Sci. Eng. A 663 (2016) 78–85.

[7] H. Zare, M. Jahedi, M.R. Toroghinejad, M. Meratian, M. Knezevic, Microstructure and mechanical properties of carbon nanotubes reinforced aluminum matrix composites synthesized via equal-channel angular pressing, Mater. Sci. Eng. A 670 (2016) 205–216.

[8] R.P. Bustamante, F.P. Bustamante, I.E. Guel, C.R.S. Rodriguez, J.A.M. Aquino, J.M.H. Ramirez, et al., Characterization of Al2024-CNTs composites produced by mechanical alloying, Powder Technol. 212 (2011) 390–396.

[9] Z.Y. Liu, B.L. Xiao, W.G. Wang, Z.Y. Ma, Singly dispersed carbon nanotube/aluminum composites fabricated by powder metallurgy combined with friction stir processing, Carbon 50 (2012) 843–852.

[10] N. Saheb, Compressive behavior of spark plasma sintered CNT reinforced Al2124 and Al6061 nanocomposites, Adv. Mater. Res 652 (2013) 33–37.

[11] Y.V.R.K. Prasad, Processing maps: a status report, J. Mater. Eng. Perfom 12 (2003) 638–645.

[12] S. Wang, L.G. Hou, J.R. Luo, J.S. Zhang, L.Z. Zhuang, Characterization of hot workability in AA7050 aluminum alloy activation energy and 3-D processing map, J. Mater. Proc. Technol. 225 (2015) 110–121.

[13] Y. Wang, J. Peng, L. Zhong, F. Peng, Modeling and application of constitutive model considering the compensation of strain during hot deformation, J. Alloy Compd. 681 (2016) 45570.

[14] C. Shi, J. Lai, X.G. Chen, Microstructural evolution and dynamic softening mechanisms of Al-Zn-Mg-Cu alloy during hot compression deformation, Materials 7 (244) (2014) 64.

[15] L. Chen, G. Zhao, J. Gong, X. Chen, M. Chen, Hot deformation behaviors and processing maps of 2024 aluminum alloy in as-cast and homogenized state, J. Mater. Eng. Perform. 24 (2015) 5002–5012.

[16] C. Shi, X.G. Chen, Evolution of activation energies for hot deformation of 7150 aluminum alloys with various Zr and V additions, Mater. Sci. Eng. A 650 (2016) 197–209.

[17] C. Shi, W.M. Mao, X.G. Chen, Evolution of activation energy during hot deformation of AA7150 aluminum alloy, Mater. Sci. Eng. A 517 (2013) 83–91.

[18] F. Khan MD, S.K. Panigrahi, Achieving excellent thermal stability and very high activation energy in an ultrafine-grained magnesium silver rare earth alloy prepared by friction stir processing, Mater. Sci. Eng. A 675 (2016) 338–344.

[19] B.C. Ko, Y.C. Yoo, Prediction of dynamic recrystallization condition by deformation efficiency for Al2024 composite reinforced with SiC particle, J. Mater. Sci. 35 (2000) 4073–4077.

[20] N.P. Jin, H. Zhang, Y. Han, W.X. Wu, J.H. Chen, Hot deformation behavior of 7150 aluminum alloy during compression at elevated temperature, Mater. Charact. 60 (2009) 530–536.

[21] S. Wang, J.R. Luo, J.S. Zhang, L.Z. Zhuang, Identification of the threshold stress and true activation energy for characterizing the deformation mechanisms during hot working, Mater. Des. 113 (2017) 27–36.

[22] F. Mokdad, D.L. Chen, Z.Y. Liu, B.L. Xiao, D.R. Ni, Z.Y. Ma, Deformation and strengthening mechanisms of a carbon nanotube reinforced aluminum composite, Carbon 104 (2016) 64–77.

[23] J. Liao, M.J. Tan, R.V. Ramanujan, S. Shukla, Carbon nanotube evolution in aluminum matrix during composite fabrication process, Mater. Sci. Forum 690 (2011) 294–297.

[24] S. Suarez, E.R. Moore, B. Lechthaler, F. Mucklich, Grain growth analysis of multiwalled carbon nanotube-reinforced bulk Ni composites, Carbon 70 (2014) 173–178.

[25] W.S. Miller, F.J. Humphreys, Strengthening mechanisms in particulate metal matrix composites, Scr. Mater. 25 (1991) 33–38.

[26] K.T. Kim, J. Eckert, S.B. Menzel, T. Gemming, S.H. Hong, Grain refinement assisted strengthening of carbon nanotube reinforced copper matrix nanocomposites, Appl. Phys. Lett. 92 (2008) 121901.

[27] I. Daigo, Y. Terada, T. Sato, Effect of calcium additions on creep properties of a die-cast AM50 magnesium alloy, Mater. Trans. 49 (2008) 1957–1962.

[28] H.J. Choi, J.H. Shin, B.H. Min, J. Park, D.H. Bae, Reinforcing effects of carbon nanotubes in structural aluminum matrix nanocomposites, J. Mater. Res. 24 (2009) 2610–2616.

[29] A.A. Khamei, K. Dehghani, R. Mahmudi, Modeling the hot ductility of AA6061 aluminum alloy after severe plastic deformation, JOM 67 (2015) 966–972.

[30] J.G. Park, D.H. Keum, Y.H. Lee, Strengthening mechanisms in carbon nanotube-reinforced aluminum composites, Carbon 95 (2015) 690–698.

[31] K. Zhu, C. Jiang, Z. Li, L. Du, Y. Zhao, Z. Chai, et al., Residual stress and microstructure of the CNT/6061 composite after shot peening, Mater. Des. 107 (2016) 333–340.

[32] C.M. Sellars, W.J. McTegart, On the mechanism of hot deformation, Acta Metall. 14 (1966) 1136–1138.

[33] H.J. McQueen, N.D. Ryan, Constitutive analysis in hot working, Mater. Sci. Eng. A 322 (2002) 43–46.

[34] N. Tahreen, D.F. Zhang, F.S. Pan, X.Q. Jiang, D.Y. Li, D.L. Chen, Hot deformation and processing map of an as-extruded Mg-Zn-Mn-Y alloy containing I and W phases, Mater. Des. 87 (2015) 245–255.

[35] J.C. Malas, S. Venugopal, Seshacharyulu. Effect of microstructural complexity on the hot deformation behavior of aluminum alloy 2024, Mater. Sci. Eng. A 368 (2004) 41–47.

[36] S.K. Shaha, F. Czerwinski, W. Kasprzak, J. Friedman, D.L. Chen, Effect of Zr, V and Ti on hot compression behavior of the Al-Si cast alloy for powertrain applications, J. Alloy Compd. 615 (2014) 1019–1031.

[37] C. Li, S. Wang, D. Zhang, S. Liu, Z. Shan, X. Zhang, Effect of Zener-Hollomon parameter on quench sensitivity of 7085 aluminum alloy, J. Alloy Compd. 688 (456) (2016) 62.

[38] L. Xiao, D.L. Chen, M.C. Chaturvedi, Shearing of γ" precipitates and formation of planar slip bands in Inconel 718 during cyclic deformation, Scr. Mater. 52 (2005) 603–607.

[39] H. Ahamed, V. Senthilkumar, Hot deformation behavior of mechanically alloyed Al6063/0.75Al₂O₃/0.75Y₂O₃ nano-composite-a study using constitutive modeling and processing map, Mater. Sci. Eng. A 539 (2012) 349–359.

[40] M. Voncina, J. Medved, T. Boncina, F. Zupanic, Effect of Ce on morphology of α(Al)-Al₂Cu eutectic in Al-Si-Cu alloy, Trans. Nonfer Metal. Soc. China 24 (2014) 36–41.

[41] L. Lasa, J.M. Rodriguez-Ibabe, Characterization of the dissolution of the Al₂Cu phase in two Al-Si-Cu-Mg casting alloys using calorimetry, Mater. Character 48 (2002) 371–378.

[42] J.C. Shao, B.L. Xiao, Q.Z. Wang, Z.Y. Ma, Y. Liu, K. Yang, Constitutive flow behavior and hot workability of powder metallurgy processed 20vl.%SiCp/2024Al composite, Mater. Sci. Eng. A 527 (7865) (2010) 72.

[43] S. Gangolu, A. Gourav Rao, I. Sabirov, B.P. Kashyap, N. Prabhu, V.P. Deshmukh, Development of constitutive relationship and processing map for Al-6-65Si-0.44Mg alloy and its composite with B₄C particulates, Mater. Sci. Eng. A 655 (256) (2016) 264.